AD-A114 765 ROCHESTER UNIV N Y LAB FOR LASER ENERGETICS F/G 20/5
DEVELOPMENT OF X-RAY LASER MEDIA: MEASUREMENT OF GAIN AND DEVEL--ETC(U)
FEB 82 J FORSYTH AFOSR-81-0059
UNCLASSIFIED AFOSR-TR-82-0390 NL

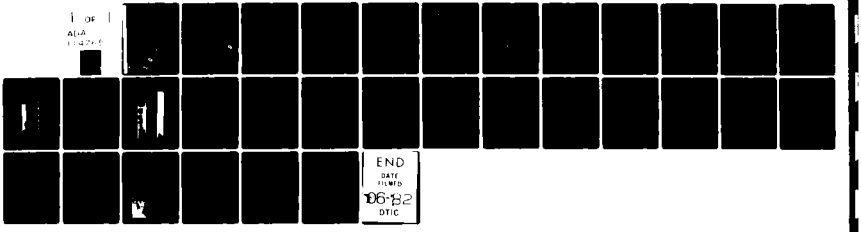

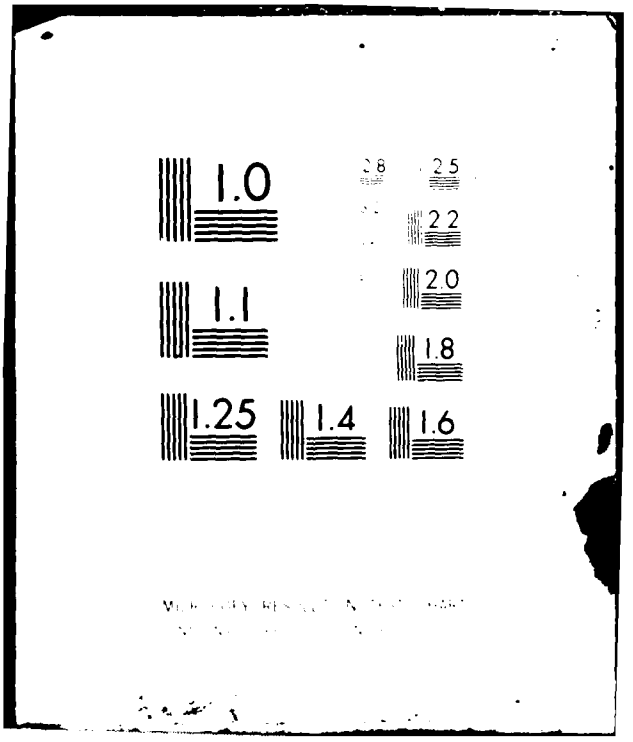
1.0
2.8
2.5
2.2
2.0
1.1
1.8
1.25
1.4
1.6

(4)

February 1982

Annual Scientific Report
1 January 1981 - 31 December 1981

Grant AFOSR 81-0059

Development of X-Ray Laser Media: measurement of Gain and Development of Cavity Resonators for Wavelengths Near 130 Angstroms

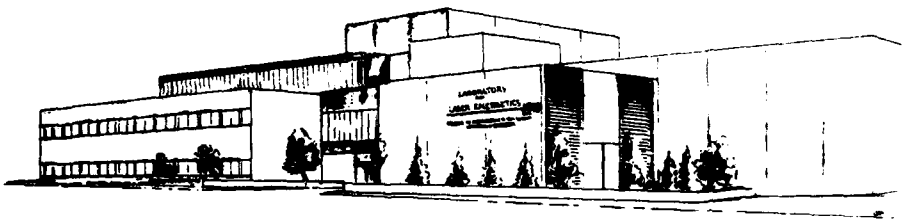

Laboratory for Laser Energetics
University of Rochester
250 East River Road
Rochester, New York 14623

UR
LLE

Unclassified

SECURITY CLASSIFICATION OF THIS PAGE (When Data Entered)

REPORT DOCUMENTATION PAGE	READ INSTRUCTIONS BEFORE COMPLETING FORM
1. REPORT NUMBER: AFOSR-TR- 82-0390	2. GOVT ACCESSION NO. AD-A114 [illegible] / 3. RECIPIENT'S CATALOG NUMBER
4. TITLE (and Subtitle): DEVELOPMENT OF X-RAY LASER MEDIA: MEASUREMENT OF GAIN AND DEVELOPMENT OF CAVITY RESONATORS FOR WAVELENGTHS NEAR 130 ANGSTROMS	5. TYPE OF REPORT & PERIOD COVERED: Annual Scientific Report 1/1/81 - 12/31/81 / 6. PERFORMING ORG. REPORT NUMBER
7. AUTHOR(s): Dr. James Forsyth	8. CONTRACT OR GRANT NUMBER(s): AFOSR 81-0059
9. PERFORMING ORGANIZATION NAME AND ADDRESS: Laboratory for Laser Energetics, College of Engineering and Applied Science, University of Rochester, 250 E. River Rd., Rochester, New York 14623	10. PROGRAM ELEMENT, PROJECT, TASK AREA & WORK UNIT NUMBERS: 2301/A8 61102F
11. CONTROLLING OFFICE NAME AND ADDRESS: Air Force Office of Scientific Research, Bolling Air Force Base, Washington, D. C. 20332	12. REPORT DATE: Feb. 1982 / 13. NUMBER OF PAGES: 30
14. MONITORING AGENCY NAME & ADDRESS(if different from Controlling Office)	15. SECURITY CLASS. (of this report): Unclassified / 15a. DECLASSIFICATION DOWNGRADING SCHEDULE

16. DISTRIBUTION STATEMENT (of this Report)

~~Unclassified~~ Approved for public release; distribution unlimited.

17. DISTRIBUTION STATEMENT (of the abstract entered in Block 20, if different from Report)

18. SUPPLEMENTARY NOTES

19. KEY WORDS (Continue on reverse side if necessary and identify by block number)

X-Ray, Reflectors, Laser, Plasma

20. ABSTRACT (Continue on reverse side if necessary and identify by block number)

Experiments showing improved levels of population inversion on soft x-ray transitions in laser heated plasmas were performed with a frequency tripled ND^{+3}: glass laser facility. Optics have been fabricated which will allow line focus experiments to be performed with this facility in 1982. Design studies on soft x-ray cavity reflectors have continued.

DD FORM 1 JAN 73 1473 EDITION OF 1 NOV 65 IS OBSOLETE

Unclassified

SECURITY CLASSIFICATION OF THIS PAGE (When Data Entered)

1.0 SUMMARY OF RESEARCH OBJECTIVES

During the January 1 through December 31, 1981, support period we have concentrated our research in the following two areas:

1. Extension of the results of previous studies which demonstrated the existence of soft x-ray population inversions in recombining, laser-produced plasma to the development of a practical amplifier device.
2. A study of the performance which would realistically be expected to be obtained from multilayer structures suitable for use as normal incidence, soft x-ray cavity mirrors.

Our activities during this period have led to several significant achievements:

1. Demonstration of substantially enhanced population inversion levels in point focus, step-target geometry due to the use of frequency tripled glass laser radiation to initially heat the plasma medium.
2. Construction of cylindrical focussing plates for the ultraviolet (frequency tripled) laser pulses to enable line focus experiments to begin in 1982.
3. Successful modelling of the pc... ...us experimental observations in aluminum plasmas using the one-dimensional, laser plasma hydrodynamic computer code, LILAC.

4. Modelling of the role of various probable fabrication defects in the predicted performance of multilayer reflector devices for soft x-ray laser cavities.

An elaboration of these achievements will constitute the main body of this report.

2.0 STATUS OF THE RESEARCH

2.1 Soft X-Ray Amplifier Development

The essential idea behind our approach to building a soft x-ray laser is to create a hot, high density, highly ionized plasma which is converted into a recombining plasma in a suitable expansion geometry. We create the initial plasma conditions by focussing a high intensity light pulse from a Nd^{+3}:glass laser onto a suitable solid target. During the past 18 months a significant new development in laser technology has occurred at LLE which has greatly enhanced the measured performance of such recombining plasmas in producing inverted populations. This development is the demonstration and now routine operation of a high efficiency frequency tripling system for high peak power Nd^{+3}:glass lasers. As the benefits of the use of frequency tripled, ultraviolet radiation in these experiments became clear, we modified our experimental facility for its use. In this section we will review the frequency tripling concept and compare the use of ultraviolet vs infrared radiation to heat high density plasmas. We will then directly compare the use of the two radiations in our soft x-ray population inversion experiment.

An example of the laser target irradiation geometry and the diagnostic set-up we use is given in Fig. 1. In a typical experiment a 20-50 Joule 0.5 nsec FWHM nd^{+3}: glass laser pulse is focussed onto the surface of a moderate Z slab target such as aluminum or magnesium. The target geometry is arranged to allow the expanding, hot plasma from the surface of the slab to be partially intercepted by a foil (shown here as magnesium).

The foil is postulated to provide a heat sink in the plasma expansion,[1] leading to an enhanced rate of collisional recombination for the highly stripped plasma ions. Such recombination processes favor the production of states of high principal quantum number, leading to population inversion.[2] The inversion process is shown schematically in Fig. 2. During the past year we have conducted experiments under conditions which lead to a substantially increased density of inverted population on 4→3 transitions in helium-like ions of the slab material (e.g. aluminum or magnesium). These experiments, described in the next section, greatly increase the chances for a successful soft x-ray gain demonstration in the next year.

The frequency tripling scheme has been described in a series of papers.[3,4,5] The linearly polarized output of a Nd^{+3}:glass laser is incident on a Type II KDP crystal which is angle-timed for optimum phase matching. The input polarization is set at 35^0 with respect to the ordinary ray direction in the crystal instead of the usual 45^0, resulting in SHG efficiencies near 67% for a broad range of input intensities.

EXPERIMENTAL CONFIGURATION FOR MEASURING POPULATION INVERSION

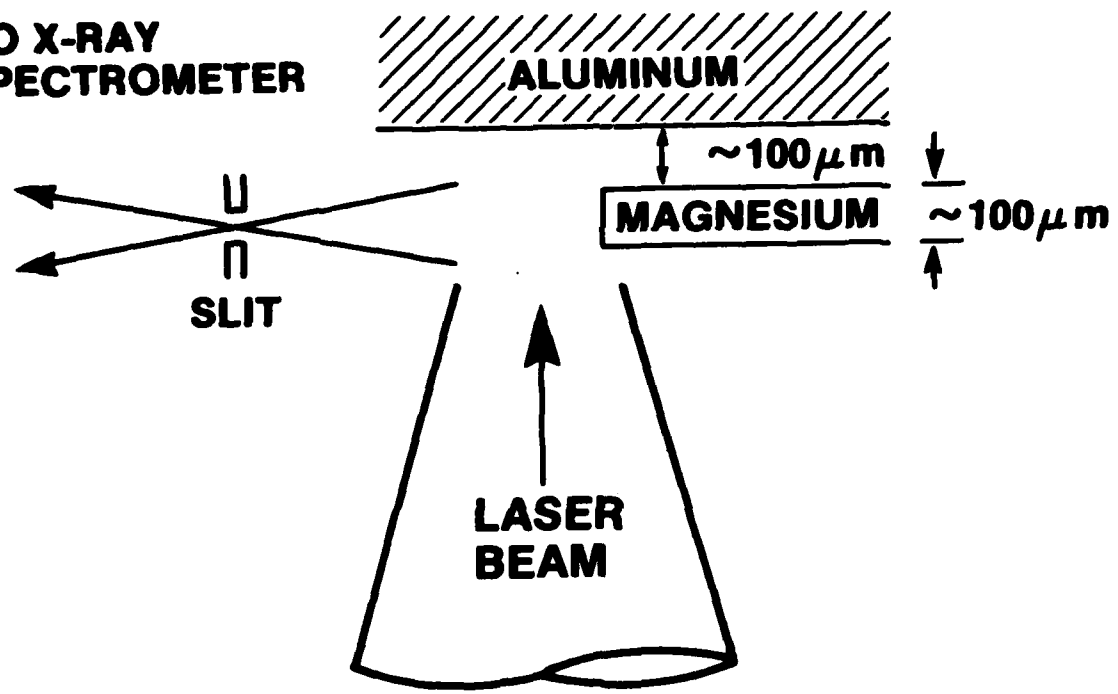

X49

Figure 1

SCHEME FOR AN X-RAY AMPLIFIER

UR LLE

Laser-Produced Plasma

High T_e , High N_e

Cooling ↓ **("heat sink" foil)**

Low T_e , High N_e

↕

Collisions (3-body recombination)
Dominate radiative processes

↓

"4-level" system

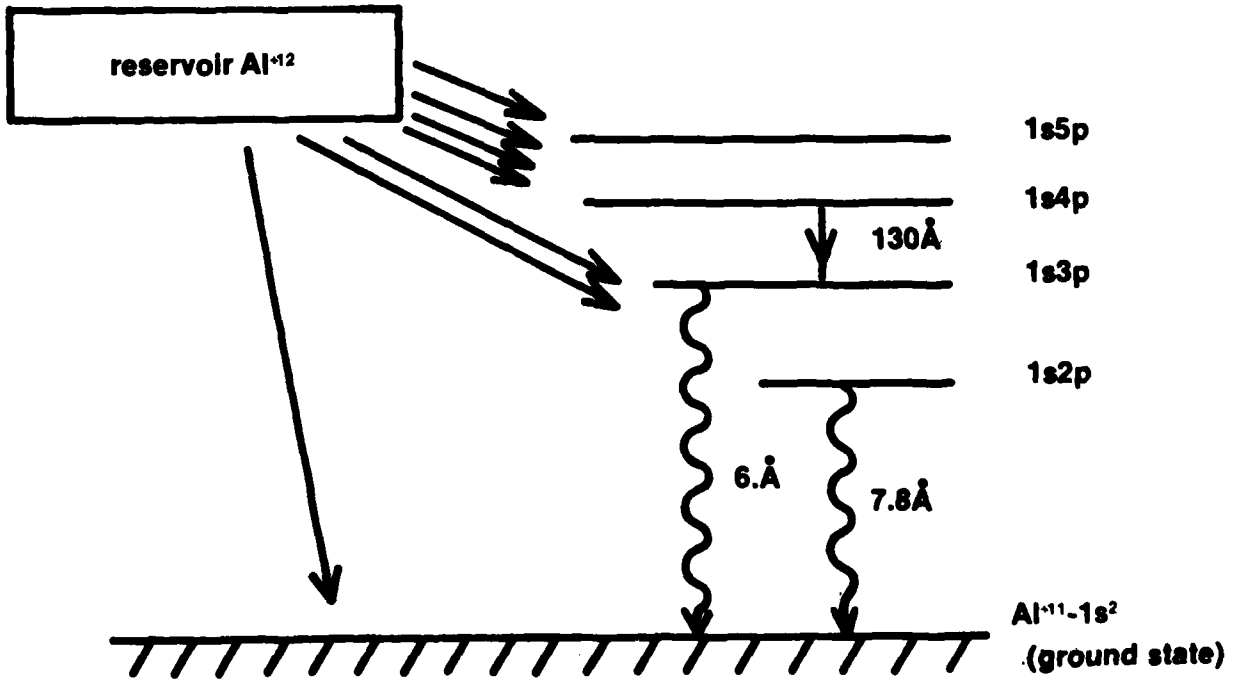

Figure 2

X196

The light emerging from the doubling crystal thus consists of a 1:1 photon mix of fundamental and second harmonic with orthogonal polarizations. These radiations then enter a Type II KDP mixing crystal with optimum mix and polarization for efficient third harmonic generation. The crystal and polarization vector orientations are shown in Fig. 3. Routine overall conversion rates to third harmonic of 60% or more are achieved at 127 mm aperture in the system used on our glass development laser facility. In 0.5 nsec pulses, between 40 and 50 Joules of 0.351 μm radiation are delivered to targets, resulting in on-target intensities of 10^{15} W/cm^2.

A systematic study of many aspects of laser target interaction physics at 0.35 μm has been conducted over the past year. Many results of these studies are published,[6,7] or in-press. We will summarize the relevant features of ultraviolet (third harmonic) irradiation compared to infrared irradiation of targets under otherwise similar conditions. For on-target intensities in the vicinity of 10^{15} W/cm^2 we find

1. The UV absorption is much higher than the IR absorption (typically 75% vs 30%).
2. The UV absorption is classical (collisional) as opposed to resonance absorption in the IR. There is no suprathermal electron distribution or suprathermal energy transport with UV irradiation.

EFFICIENT CONVERSION TO SHORTER WAVELENGTH IS POSSIBLE USING NON-LINEAR CRYSTALS

UR LLE

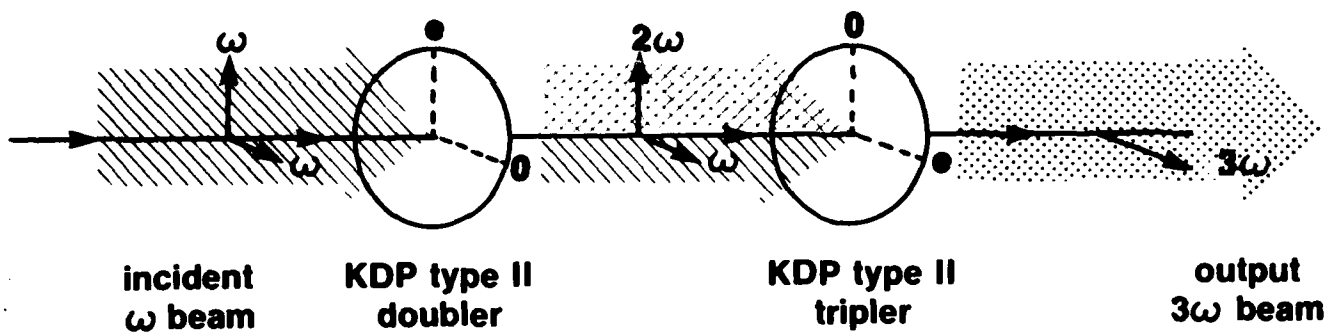

Figure 3

E943

3. The UV absorption occurs at higher electron density ($\sim 10^{22}$ cm^{-3}) than the IR absorption ($\sim 10^{21}$ cm^{-3}).
4. The plasma coronal electron temperature is the same or slightly higher with UV irradiation (1-2 keV).
5. Both soft x-ray line and continuum emission increases by an order of magnitude or more with UV irradiation compared Joule for Joule with the IR.

These observations suggested that frequency tripled Nd^{+3}:glass laser radiation would be advantageous for use in our population inversion experiments. In particular, it appeared that we could vary one of our initial conditions - the plasma particle density - while leaving the initial temperature and the expansion geometry unchanged. The absence of hot electrom production would also help to carify the role of the plate we employ in the expanding plasma. If the role of the plate is strictly geometricaly or thermal in nature then it is possible that our density of inverted population might be increased.

To implement the conversion to frequency tripled light in our experiment, our laser beam transport optics were recoated for 0.351 μm, the vacuum window to our experimental chamber was replaced by a coated, fused silica window, and our focussing lens was replaced by a single element f/12 fused silica lens. Alignment of the UV system is accomplished with the aid of a CW argon ion laser operating at 0.355 μm. This CW beam is inserted into the beam transport system at the point where the

IR laser enters the frequency conversion system. A schematic diagram of the frequency tripling system, the alignment system and the beam diagnostics is given in Fig. 4.

We now present some comparative results on step-target experiments using IR and UV irradiation under otherwise similar conditions. In these experiments a target geometry similar to that shown in Fig. 1 was used except that the foil was arranged in the form of two half-planes, i.e. a slit. The spatially resolving crystal spectrograph, set to record transitions to the ground state of helium-like and hydrogen-like target ions, was positioned to view along the open axis of the slit.

In Fig. 5 we present two spatially resolved spectra from aluminum targets heated by 50 Joules, 600 psec FWHM pulses of 1.054 μm laser radiation, recorded using a flat TAP crystal spectrograph with a spatially resolving slit. The equivalent source space dimensions for our geometry are shown on the figure. A lead foil slit was used in the target producing the left hand spectrum. This foil was convenient in that it produces no strong emission lines in this part of the spectrum. A similar expansion spectrum is observed in the right hand spectrum, obtained from an aluminum target fitted with a thick magnesium slit in the form of a channel. Because of the close proximity of many of the magnesium and aluminum lines is it difficult to perform line ratio analysis for temperature and density profile reconstruction. However, the use of lead foil targets consistently produced severe damage on the laser focussing optics due to production of high velocity lead debris along the plasma expansion direction.

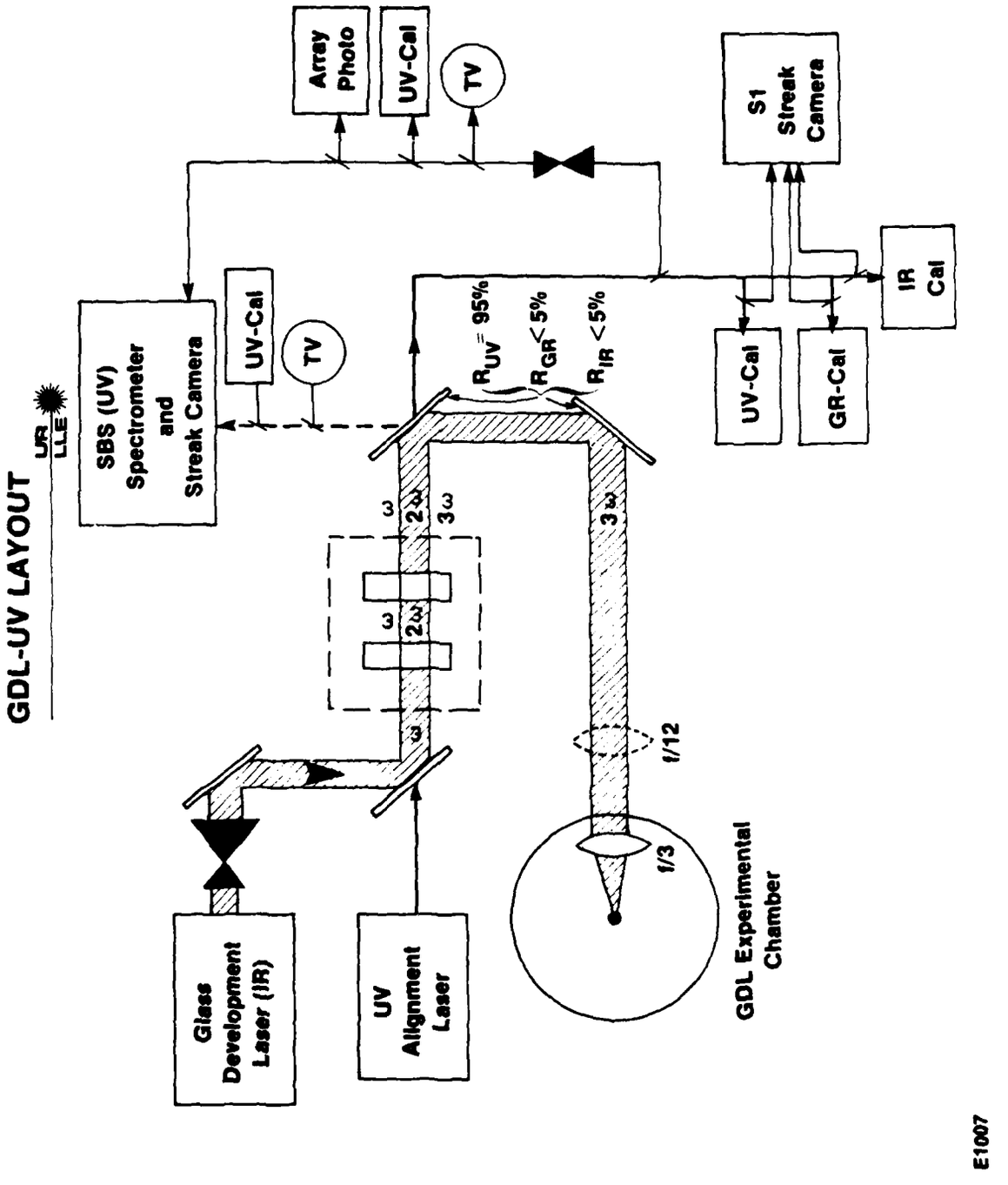
GDL-UV LAYOUT
UR
LLE
Array Photo
UV-Cal
TV
S1 Streak Camera
IR Cal
SBS (UV) Spectrometer and Streak Camera
UV-Cal
TV
$R_{UV} \geq 95\%$
$R_{GR} < 5\%$
$R_{IR} < 5\%$
UV-Cal
GR-Cal
3ω
2ω
3ω
3ω
3
2ω
ω
f/12
f/3
GDL Experimental Chamber
Glass Development Laser (IR)
UV Alignment Laser
E1007

Figure 4

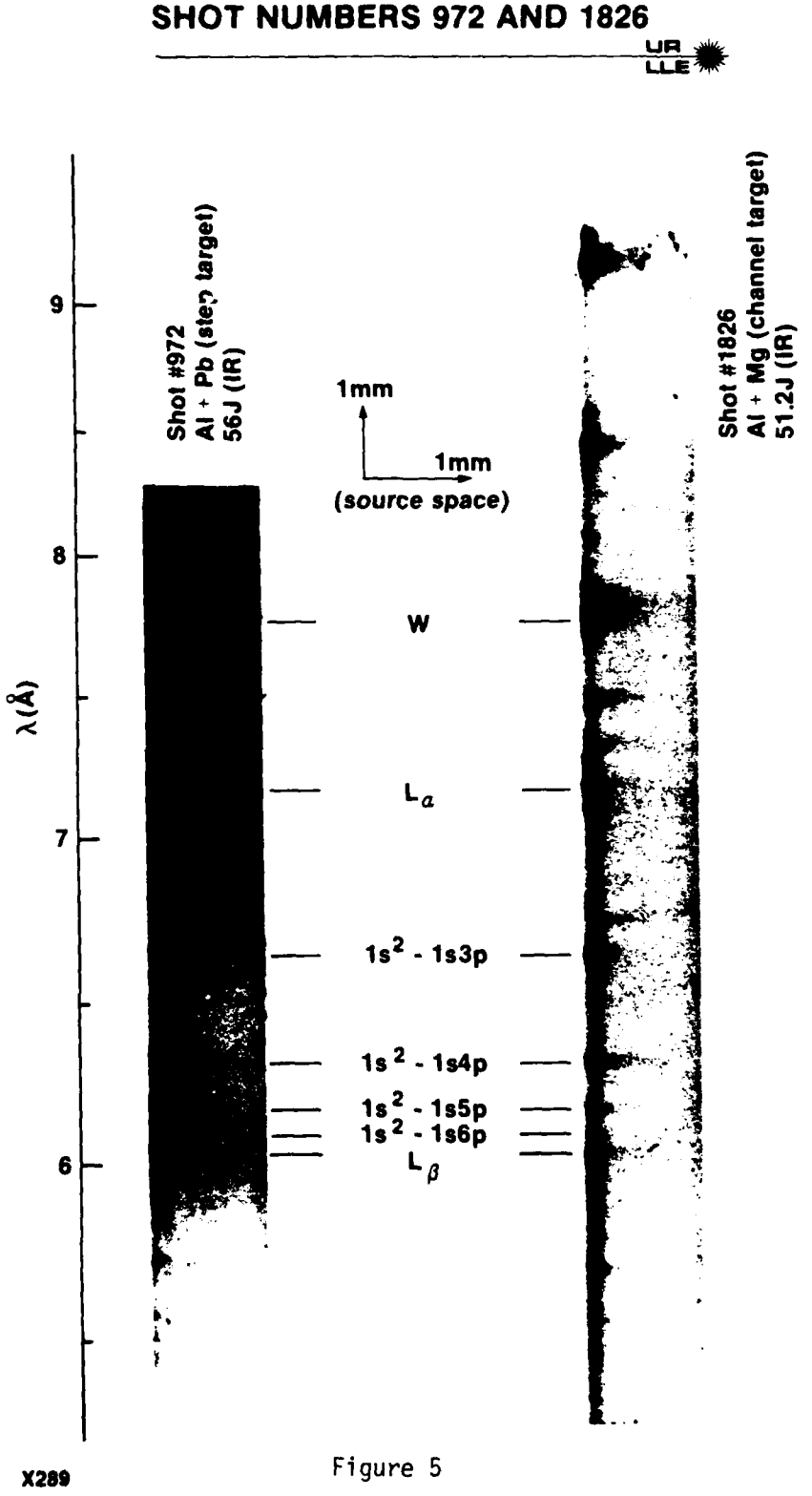
SHOT NUMBERS 972 AND 1826
UR
LLE
Shot #972
Al + Pb (step target)
56J (IR)
1mm
1mm
(source space)
Shot #1826
Al + Mg (channel target)
51.2J (IR)
9
8
7
6
λ(Å)
W
L_α
$1s^2$ - 1s3p
$1s^2$ - 1s4p
$1s^2$ - 1s5p
$1s^2$ - 1s6p
L_β
X289

Figure 5

In Fig. 6 we present two spatially resolved spectra from aluminum targets heated by 20 Joule, 490 psec FWHM pulses of 0.351 μm laser radiation, recorded on the same crystal spectrograph as used to record Fig. 5 except that an additional 0.75 μ aluminum foil filter reduces the greatly increased x-ray emission intensities with the UV irradiation. The equivalent source space dimensions are shown on the figure. The left hand spectrum was produced by a target with a titanium foil slit while the right hand spectrum was produced by a target with a magnesium foil slit. A slight misalignment of the spatially resolving crystal spectrograph axis with respect to the open axis of the target slit is evident in this figure. The two spectra show very similar expansion characteristics, indicating that the performance of these targets in the UV is essentially independent of the heat sink material just as has been observed for IR irradiation.

The spectra shown in Figs. 5 and 6 are presented on nearly identical spatial scales and recorded optical densities. It is immediately striking that the length of expanding plasma column giving rise to intense radiation from the $n \rightarrow 1$ transitions is much greater with UV target irradiation. This is consistent with the coupling of UV radiation and hot plasma formation at much higher particle density than with IR. Densitometric scans of the spectra in Fig. 6 show a clearly defined inversion in the intensity of the $4 \rightarrow 1$ over the $3 \rightarrow 1$ transitions in the helium-like

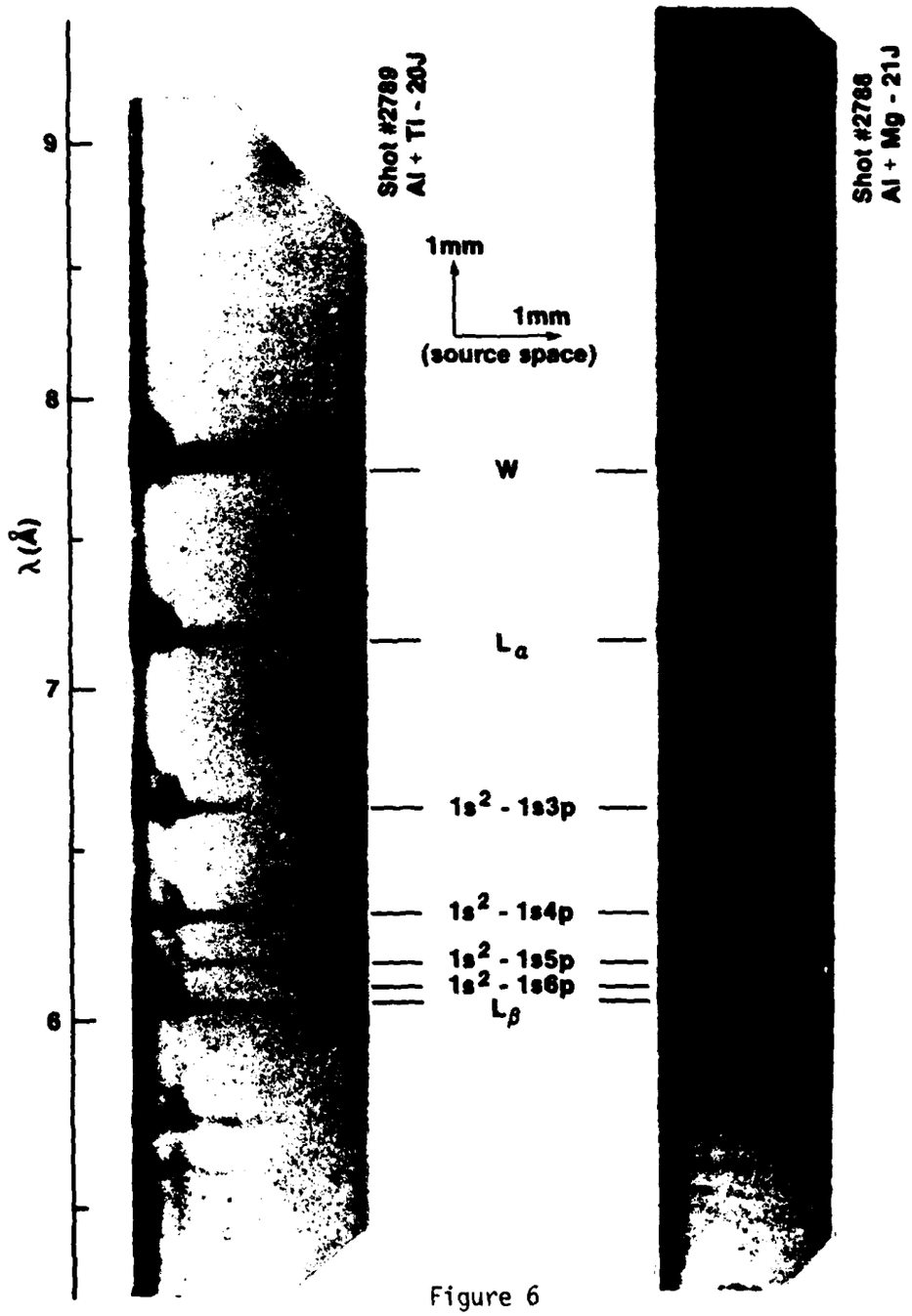
SHOT NUMBERS 2789 AND 2788
Shot #2789
Al + Ti - 20J
Shot #2788
Al + Mg - 21J
1mm
1mm
(source space)
9
8
7
6
λ(Å)
W
L_α
$1s^2$ - 1s3p
$1s^2$ - 1s4p
$1s^2$ - 1s5p
$1s^2$ - 1s6p
L_β
X280

Figure 6

aluminum ion beginning between 600 and 900 μm from the initial target surface, roughly 2-3 times farther out than is seen in the IR experiments. Based on the absolute intensity calibration of our spectrograph we calculate the density of inverted population on the 4 → 3 transition would be 3-5 times higher in these UV experiments than in any of our IR measurements.

As a result of our decision to convert our experimental system to ultraviolet irradiation, we postponed our procurement of a cylindrical focussing lens for line focus experiments. The improved performance of the recombining plasmas with ultraviolet irradiation has motivated us to redesign our cylindrical focussing system for the ultraviolet. The f/12 spherical focussing lens has a focal length of approximately 1660 mm. This is sufficiently long to permit the use of additional weak cylindrical plates to obtain a line focus. By employing two such plates we may obtain continuous control over the aspect ratio of the line focus by rotation of their respective cylinder axes. A pair of fused silica plates has been fabricated for this purpose. These plates are currently deployed in preliminary line focus experiments.

Because of the essentially classical behavior of intense, focussed, ultraviolet laser pulses in plasma media, we felt that for the first time we might hope to model the experiments on production of population inversion described above. Accordingly, in our first such efforts we sought to adapt a highly developed numerical plasma hydrodynamic code, LILAC, to the description of the observed, time integrated, spatially resolved emission spectrum from the plasma ions. LILAC calculates inverse bremstrahlung absorption for an electromagnetic wave propagation through a one dimensional (i.e. spherically symmetric) plasma. The hydrodynamic equations of continuity,

and energy and momentum conservation are then solved at each point during each small, adjustable time interval. The temperatures of electron and ion populations are calculated separately, and energy exchange between populations is provided for in each computational cell. The various coronal species are assumed to behave in an ideal gas fashion. The degree of ionization is calculated at each step using the model appropriate to the plasma conditions.

To enable a one-dimensional code to accurately replicate observations made on flat target experiments, it has been found effective to assume an irradiation/target geometry shown in Fig. 7. If the diameter of the laser focal spot on the flat target is ϕ then a spherical target radius of 2ϕ is chosen in the calculation. The expansion of the plasma proceeds radially from the surface in a pie-shaped region.

The emission spectrum is obtained using a rate equation package which is calculated as a post-processing routine on LILAC. The excitation and recombinaton coefficients for the helium-like and hydrogen-like species are adapted from McWhirter and Hearn. Only ionization ground state populations are calculated for lower stages of ionization. The calculations are suppressed at all points for which the electron temperature drops below 60ev due to the lack of good data available for the species and levels of interest at such energies.

To replicate the observations of our spatially resolving spectrograph, the expanding plasma is divided into a series of laminar layers, 10 μm thick, oriented in the direction of observation. The radiation from each laminar segment (assumed to be distinguishable in our instrument) is calculated, taking into account the opacity of each ground state transition using the model of Elton. Each simulation yields a time- and

EQUIVALENT TARGET IRRADIATION GEOMETRY USED IN ONE-DIMENSIONAL *(LILAC)* SIMULATION

UR LLE

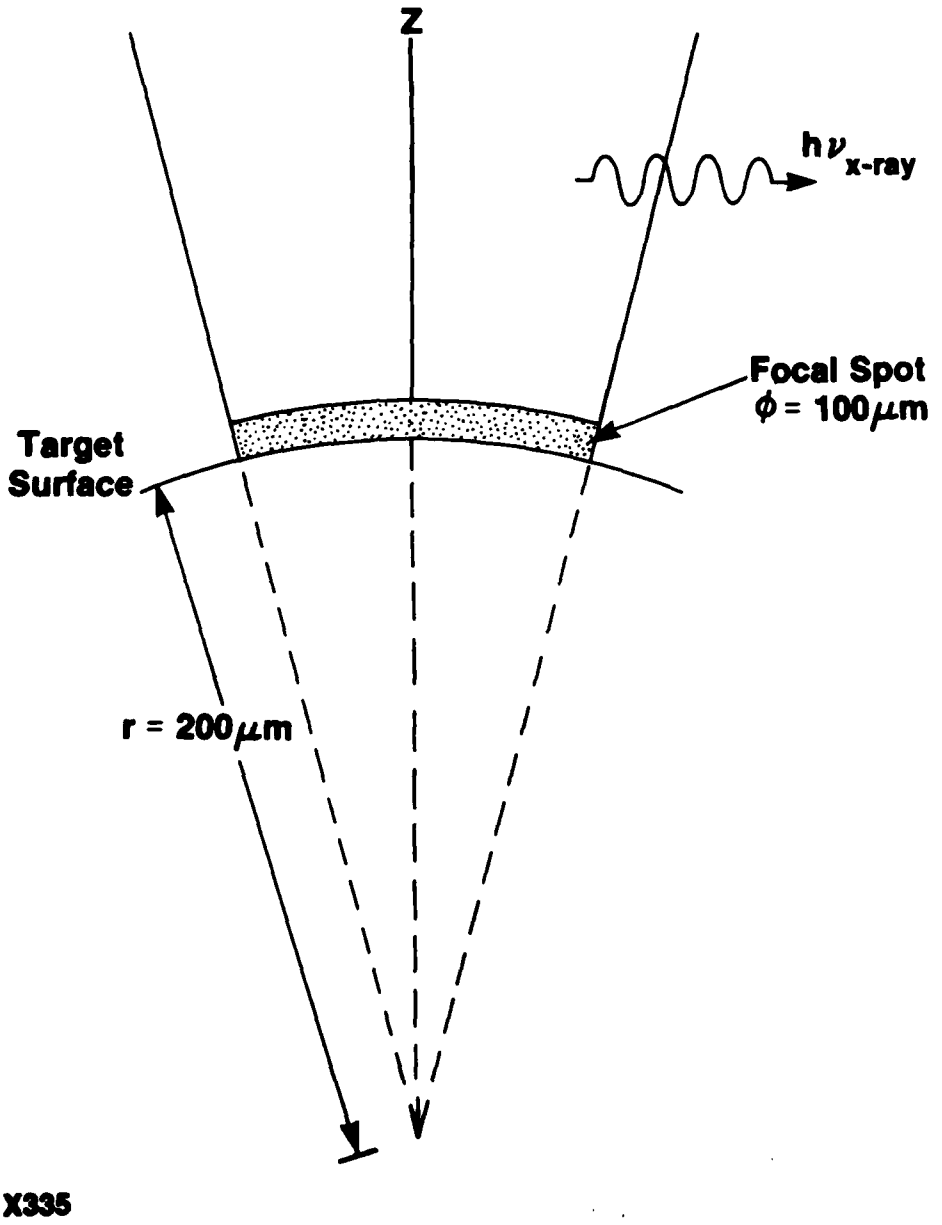

Figure 7

space-resolved spectral emission distribution as well as a time-integrated, space-resolved distribution.

To simulate the effect of the foil structure in the step-target experiments, we add a spatially dependent energy loss term to the hydrodynamic equations in the code, in thich the cooling time, τ_c, is an adjustable parameter. In this way the results could be compared to a particular physical model of the transfer of energy from the plasma to the cooling plates or foils.

In Fig. 8 we present a calculation of the time-integrated, spatially resolved emission from the 4 → 1 and 3 → 1 transitions in helium-like aluminum. In this simulation, a peak irradiation intensity of 5×10^{14} W/cm^2 at 0.351 μm was assumed with a focal spot diameter of 100 μm. A cooling plate 100 μm thick was located 200 μm from the initial target surface. The laser pulsewidth was 500 psec and assumed to be gaussian.

A "normal" line intensity distribution is exhibited close to the initial target surface. At a distance of approximately 700 μm from the target the two intensities have become equal and beyond that point they are inverted. This behavior is in very good agreement with the experimental observations presented earlier. To obtain this result a cooling time, τ_c, of 30 psec was used in the calculation. It appears that the exact value chosen for τ_c is not critical. For τ_c = 10 psec, the increase in line emission in the vicinity of the cooling plate appears to be somewhat larger than observed. For τ_c > 100 psec the lower temperature drop substantially reduces the emission from this region.

The initial success of this modelling effort is very encouraging. During the current support period we plan to continue this effort to see if further refinement and optimization of the experimental conditions can be verified.

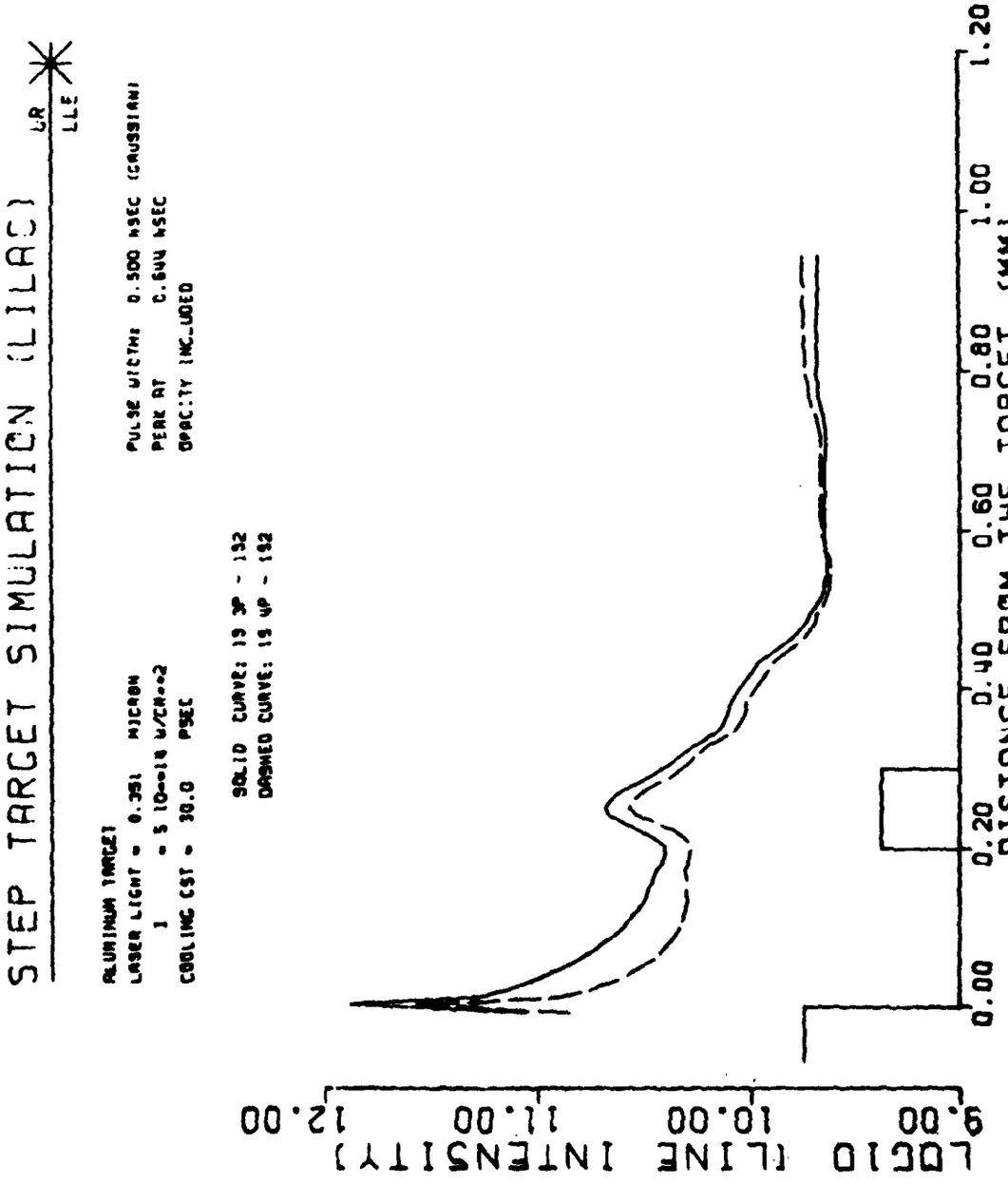
STEP TARGET SIMULATION (LILAC)
UR
LLE
ALUMINUM TARGET
LASER LIGHT = 0.351 MICRON
I = 5 10**14 W/CM**2
COOLING CST = 30.0 PSEC
PULSE WIDTH: 0.500 NSEC (GAUSSIAN)
PEAK AT 0.6NN NSEC
OPACITY INCLUDED
SOLID CURVE: 19 3P - 132
DASHED CURVE: 19 4P - 132
LOG10 (LINE INTENSITY)
9.00
10.00
11.00
12.00
0.00
0.20
0.40
0.60
0.80
1.00
1.20
DISTANCE FROM THE TARGET (MM)

Figure 8

2.2 Soft X-ray Cavity Development

Since we began our study of periodic structures which could be suitable for use as reflecting elements in a soft x-ray laser cavity, considerable activity has been initiated in several laboratories in the development of such elements.[8] Substantial variation in the technical approach to fabrication of such elements currently exists and at least one attempt at commercial manufacture may soon be realized.[9] During the past year we have generalized our analysis of the performance which could be expected from such elements to include a treatment of the effects of various structure defects and fabrication errors. Interim results of this work, which is continuing at present, are presented in the attached publication reprints and present a fair summary of the work performed during the support period.

2.3 References

1. V. A. Bhagavatula, B. Yaakobi, Opt. Comm., 24, 3, March 1978, p. 331.

2. L. I. Gudzenko and L. A. Shelepin, Soviet Physics Doklady 10, 147 (1965).

3. R. S. Craxton, "Theory of High Efficiency Third Harmonic Generation of High Power Nd:Glass Laser Radiation," Opt. Commun. 34, 474-478 (September 1980).

4. W. Seka, S. Jacobs, J. Rizzo, R. Boni, and R. S. Craxton, "Demonstration of High Efficiency Third Harmonic Conversion of High Power Nd:Glass Laser Radiation," Opt. Commun., 34, 3, 469-473 (September 1980).

5. R. S. Craxton, "High Efficiency Tripling Schemes for High Power Nd:Glass Lasers," IEEE J. Quantum Electronics QE-17, No. 9, 1981 (in-press); also, W. Seka, J. M. Soures, S. Jacobs, L. Lund, and R. S. Craxton, IEEE J. Quantum Electronics QE-17, No. 9, 1981 (in-press).

6. B. Yaakobi, T. Boehly, P. Bourke, Y. Conturie, R. S. Craxton, J. Delettrez, J. M. Forsyth, R. D. Frankel, L. M. Goldman, R. L. McCrory, M. C. Richardson, W. Seka, D. Shvarts, and J. M. Soures, "Characteristics of Target Interaction with High Power UV Laser Radiation," Optics Communications, 39, 175 (1981).

7. B. Yaakobi, P. Bourke, Y. Conturie, J. Delettrez, J. M. Forsyth, R. D. Frankel, L. M. Goldman, R. L. Mccrory, W. Seka, and J. M. Foures, "High X-Ray Conversion Efficiency with Target Irradiation by a Frequency Tripled Nd:Glass Laser," Optics Communications 38, 196 (1981).

8. E. Spiller, "Evaporated Multilayer Dispersion Elements for Soft X-Rays," AIP Conf. Proc. 75, 124 (1981); also T. W. Barbee, Jr., "Sputtered Layered Synthetic Microstructure (LSM) Dispersion Elements," AIP Conf. Proc. 75,131 (1981).

The Reflecting Properties of Soft X-Ray Multilayers

Alan E. Rosenbluth and J. M. Forsyth

Laboratory for Laser Energetics, University of Rochester, 250 East River Rd., Rochester, N.Y. 14623

ABSTRACT

We treat a variety of problems in the theory of soft x-ray multilayer mirrors. A characteristic matrix solution to Maxwell's equations is presented that applies to both periodic and non-periodic reflectors whose layers can possess arbitrary index gradients. Procedures are derived to maximize multilayer reflectivity in the kilovolt and sub-kilovolt regime. A refractive correction to Bragg's law is derived that includes the effect of absorption as well as the effect of dispersion. Multilayer reflectivity in the presence of random thickness errors is treated analytically. An analytic treatment of different kinds of interfacial roughness is described. The reflecting properties of the multilayers may contain qualitative signatures that are characteristic of the different kinds of roughness. The effect of interlayer diffusion is discussed.

I. Characteristic Matrix Analysis of X-Ray Reflectors

Our analysis of x-ray multilayers proceeds from a solution to Maxwell's material equations, given that the multilayer structure has a spatially varying complex dielectric constant ϵ. In this respect our analysis follows the Ewald-von Laue dynamical theory of crystal diffraction. In the dynamical theory it is assumed that ϵ is three-dimensionally periodic, as in a perfect crystal. We assume that ϵ is a function only of the coordinate z normal to the multilayer surface; ϵ need not be rigorously periodic.

In this case it is known that the wave equation can be separated into ordinary differential equations, whose solutions can be put into characteristic matrix form.[1] The characteristic matrix solutions for homogeneous layers are commonly used in optical multilayer calculations.

In the visible, these differential equations must be solved numerically in the case of a general structural profile, but for the x-ray regime we have solved them analytically under the assumption that $|\epsilon - 1| \ll 1$. Essentially, we treat the material medium as giving rise to a perturbation in the vacuum fields. We now present this solution.

Let the plane of incidence be the y-z plane.

Define:

S Polarization	P Polarization
$E \equiv \hat{E}_x$	$E \equiv -\hat{E}_y/\cos\theta$
$H \equiv \hat{H}_y/\cos\theta$	$H \equiv \hat{H}_x$

(1)

The characteristic matrix solution for the Kth cell of the multilayer shown at right is:

$$\begin{pmatrix} E_{K-1} \\ H_{K-1} \end{pmatrix} = \begin{pmatrix} -\cos\phi_K - \rho_K & -i(t_K - \gamma_K) \\ -i(t_K + \gamma_K) & -\cos\phi_K + \rho_K \end{pmatrix} \begin{pmatrix} E_K \\ H_K \end{pmatrix} \qquad (2)$$

where:

$$\phi_K \equiv \pi - \frac{2\pi d_K}{\lambda}\cos\theta \qquad \gamma_K \equiv \frac{2\pi}{\lambda}\sec\theta \int_{\text{cell}} dz\, \Delta(z) \cos\left(\frac{4\pi}{\lambda}\cos\theta\, z\right)$$

$$\Delta(z) \equiv \frac{1}{2}[\epsilon(z)-1] \qquad \rho_K \equiv \frac{2\pi}{\lambda}\sec\theta \int_{\text{cell}} dz\, \Delta(z) \sin\left(\frac{4\pi}{\lambda}\cos\theta\, z\right)$$

$$\mu_K \equiv \frac{2\pi}{\lambda}\sec\theta \int_{\text{cell}} dz\, \Delta(z) \qquad t_K \equiv \sin\phi_K \cdot \mu_K \qquad (3)$$

(Here we follow the optics convention where θ is measured to the normal.)

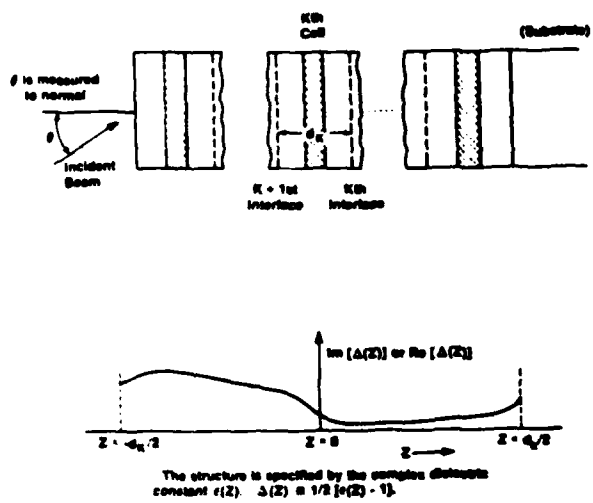

Fig. 1. Decomposition of reflector into unit cells.

We note that the structure as determined by $\Delta(z) \equiv 1/2(\epsilon(z)-1)$ need not correspond to a succession of homogeneous layers, but can have an arbitrary variation along z.

If ρ_K is the amplitude reflectivity of the stack of cells K-1, K-2, ... 1, then:

$$E_K \equiv 1 + \rho_K \qquad H_K \equiv 1 - \rho_K \qquad (4)$$

From these we can derive a difference equation that propagates the amplitude reflectance from unit cell to unit cell. This is analogous to the amplitude recursion formula that is used to propagate the reflected amplitude from single layer to single layer in optical multilayer calculations. The equation is:

$$\rho_{K+1} = e^{-2i(\phi_K - \mu_K)}\, \rho_K - (i\gamma_K - \rho_K) - (i\gamma_K + \rho_K)\, \rho_K^2 \qquad (5)$$

This equation is particularly useful in analysing non-periodic multilayers.

0094-243X/81/750280-0691.50

II. Equivalent Parameter Analysis of Periodic Reflectors

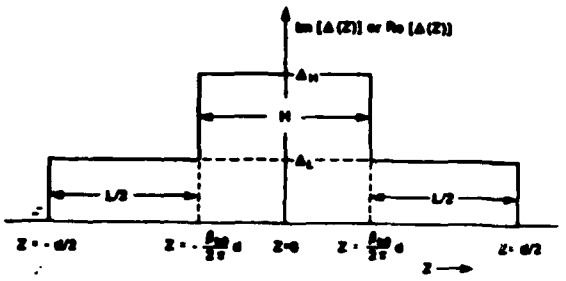

Fig. 2. Structure of unit cell in a bilayer reflector.

A multilayer with a bilayer structure consists of alternating homogeneous layers of two different materials. If the thicknesses of the different layers of each material are equal, the multilayer is periodic. By placing the cell boundaries at the midpoints of the L layers the cell structure can be made centrosymmetric as shown in the diagram above.

Then the parameter p is zero, and the characteristic matrix solution becomes:

$$\begin{pmatrix} E_{k-1} \\ H_{k-1} \end{pmatrix} = \begin{pmatrix} -1 & -(\phi-\mu-\gamma) \\ -i(\phi-\mu+\gamma) & -1 \end{pmatrix} \begin{pmatrix} E_k \\ H_k \end{pmatrix} \qquad (6)$$

where:

$$\gamma = \left(\frac{2d}{\lambda}\right)^2 (\Delta_H - \Delta_L) \sin\beta_{90}$$
$$\mu = \left(\frac{2d}{\lambda}\right)^2 [\pi\Delta_L + \beta_{90}(\Delta_H - \Delta_L)] \qquad (7)$$

This has the form of the well-known characteristic matrix solution for a single homogeneous layer having an index of refraction n_s and phase thickness β_s:[1]

$$\begin{pmatrix} E_{k-1} \\ H_{k-1} \end{pmatrix} = \begin{pmatrix} \cos\beta_s & -(i/n_s)\sin\beta_s \\ -in_s \sin\beta_s & \cos\beta_s \end{pmatrix} \begin{pmatrix} E_k \\ H_k \end{pmatrix} \qquad (8)$$

To match this matrix to the characteristic matrix for the unit cell of an x-ray reflector, eq. (6), we must make the assignments $\beta_s = \pi + \sqrt{t^2 - \gamma^2}$ and $n_s = \sqrt{(1+\gamma)/(1-\gamma)}$, where $t = \phi - \mu$. The two matricies will be equal to within first order in ϕ and Δ.

This matching of matricies is an example of what in thin film optics is known as the method of equivalent parameters.[2] There is a straightforward analogy between the properties of the single equivalent layer and the single cell of an x-ray reflector.

A reflector with J cells corresponds to a stack of J equivalent layers, which is, in effect, a single layer of phase thickness $J\beta_s$.

By letting $E_1 = 1 + \rho_1$ and $H_1 = 1 - \rho_1$, we can obtain the well-known expression for the reflectivity of a single layer:

$$\rho_{J+1} = \frac{i(n_s - 1/n_s)\tan(J\delta)}{2 - i(n_s + 1/n_s)\tan(J\delta)} \qquad (9)$$

where $\delta = \beta_s - \pi$.

This is also the reflectivity of an x-ray multilayer having J cells.

III. Optimization of Reflectivity

A computer program can be used to determine the optimum layer thicknesses in an x-ray reflector via standard optimization algorithms. A study of such optimized designs shows that if the radiation energy is above about 100 ev, a bilayer reflector that is periodic can achieve nearly the maximum reflectivity that is possible from given layer materials.

The results of the computer study agree with a theoretical analysis we have made. It can be shown analytically that if J is large, the reflectivity of an optimized periodic reflector is an extremum with respect to an arbitrary perturbation in structure. (The structures of the different cells need not be perturbed equally). This analysis neglects small terms proportional to the square of the difference of the index of refraction from one.

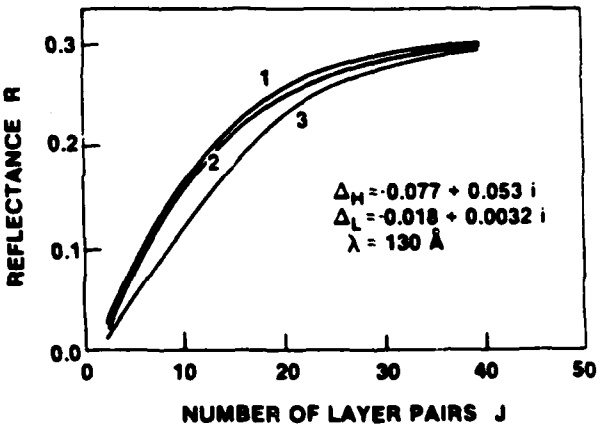

1. R (J) of non-periodic designs optimized at each J (2 J degrees of freedom)
2. R (J) of periodic designs optimized at each J (2 degrees of freedom)
3. R (J) of a periodic design optimized at J → ∞ (2 degrees of freedom)

Fig. 3. Comparison of optimization schemes.

For this reason we now concentrate on the periodic case. When J is large, the reflectivity of a periodic multilayer with a centrosymmetric structure is given by

$$\rho = -\frac{\delta + i}{\gamma} \text{ where } \delta = \sqrt{t^2 - \gamma^2} \qquad (10)$$

Let a dot represent a derivative with respect to some structural parameter. Using $\rho = -(\delta+i)/\gamma$ one can obtain a general optimization condition on the intensity reflectivity $R = \rho\rho^*$:

$$\dot{R} = 2R \cdot \mathrm{Re}\left(\frac{\dot{\rho}}{\rho}\right) = 2R \cdot \mathrm{Re}\left(\frac{\gamma\dot{\delta} - i\dot{\gamma}}{\gamma\delta}\right) = 0 \qquad (11)$$

A similar but slightly more complicated result can be obtained if $p \neq 0$.

We show below in sec. IV, eq. 16-17, that at the wavelength of peak reflectivity, δ is pure imaginary.

The condition for maximizing the peak reflectivity is therefore:

$$\mathrm{Im}\left(i - t\frac{\dot{\gamma}}{\gamma}\right) = 0 \qquad (12)$$

As an application of this result, we consider the problem of optimizing the H to L thickness ratio in a multilayer with a bilayer structure.

In order to do so we apply our optimization condition to the parameter

$$\beta_m = \frac{2\pi}{\lambda} d_H \cos\theta = \pi \frac{d_H}{d_H + d_L} \qquad (13)$$

and obtain a condition first obtained by Vinogradov and Zeldovich for the case of reflection at normal incidence:[3]

$$\tan\beta_m = \beta_m + \frac{\pi\,\mathrm{Im}(\Delta_L)}{\mathrm{Im}(\Delta_H - \Delta_L)} \qquad (14)$$

More generally, we consider mth order diffraction, and let $\beta_m = m\pi\,(d_H\ d_H{+}d_L)$. We obtain the optimization condition:

$$\tan\beta_m = \beta_m + \frac{m\pi\,\mathrm{Im}(\Delta_L)}{\mathrm{Im}(\Delta_H - \Delta_L)} \qquad (15)$$

In the plot below, and in the other numerical examples of this report, we have used preliminary values for atomic scattering factors from a forthcoming compilation.[4] These have generously been provided to us by B.Henke.

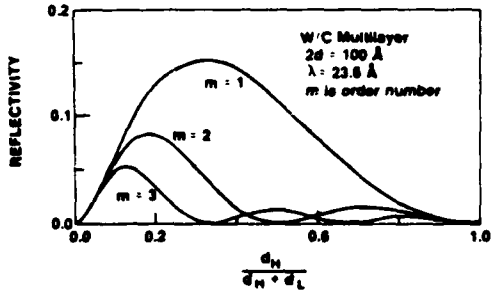

Fig. 4. Reflectivity as a function of thickness ratio.

IV. The Absorption Correction to Bragg's Law

It is well-known that the Bragg condition for crystal diffraction, $2d\cos\theta = \lambda$, must be corrected for the dispersive effects of the crystalline medium (following the optics convention, θ is the angle of incidence to the normal). It is less well-known however, that Bragg's law must be corrected for absorption as well as for dispersion.

In our formalism, the parameter ϕ represents the detuning of a multilayer from the simple Bragg angle $\theta_B \equiv \arccos(\lambda/2d)$, through the relation:

$$\phi = \frac{2\pi d}{\lambda}\left(\cos\theta_B - \cos\theta\right) \qquad (16)$$

To find the exact angle of maximum reflectivity we optimize the structure with respect to the parameter ϕ. Then using the optimization condition introduced above (eq.(11)), and setting $\dot{\gamma} = 0$, $i = 1$, we get:

$$\mathrm{Re}\,(1/\delta) = 0$$

or

$$\mathrm{Re}\,(\delta) = 0 \qquad (17)$$

The same condition is obtained in the general case when $p \neq 0$.

The requirement that $\mathrm{Re}\,(\delta) = 0$ is the same as requiring that the real part of the equivalent phase thickness β_e equal π, which is different from the usual requirement in the absence of absorption that the real part of the optical phase thickness equal π. The difference is a consequence of the presence of multiply reflected beams. In an absorbing structure, these beams undergo phase changes upon reflection, causing a phase change in the overall oscillation across each cell.

Since $\delta \equiv \sqrt{r^2 - \gamma^2}$, we can write our requirement that $\mathrm{Re}\,(\delta) = 0$ as $\mathrm{Im}\,(\delta^2) = 0$, which can be shown using the Schwarz inequality to automatically imply $\mathrm{Re}\,(\delta^2) < 0$. The condition $\mathrm{Im}\,(\delta^2) = 0$ can be manipulated to give:

$$\cos\theta_B - \cos\theta = \frac{\cos\theta_B}{\pi}\left(\mu' - \left[\frac{\gamma'\gamma'' + p'p''}{\theta\ \mu''}\right]\right) \qquad (18)$$

where primes and double-primes denote real and imaginary parts. This result was first discovered by F. Miller[5] in the context of crystal diffraction, and independently by us in the context of multilayer reflection. P. Lee, of LASL is a collaborator with us in this work.

In the usual formula for the dispersion correction, the term in square brackets is missing.[6] The first term in parentheses, μ', can be considered to represent dispersion, the term in square brackets absorption.

The relative magnitude of the two effects are compared in the plot below. The ratio plotted is

$$\mathrm{Ratio} \equiv \frac{\theta_2 - \theta_1}{\theta_B - \theta_2} \qquad (19)$$

where $\theta_B \equiv \arccos(\lambda/2d)$, θ_2 is the true Bragg angle as corrected for absorption and dispersion, and θ_1 is the Bragg angle as corrected for dispersion only.

It can be shown that the absorption correction is always smaller than the dispersion correction, but as the plot shows there are cases in which the two are comparable. The absorption correction must therefore be included whenever an accurate matching of wavelength, angle, and 2d-spacing is required.

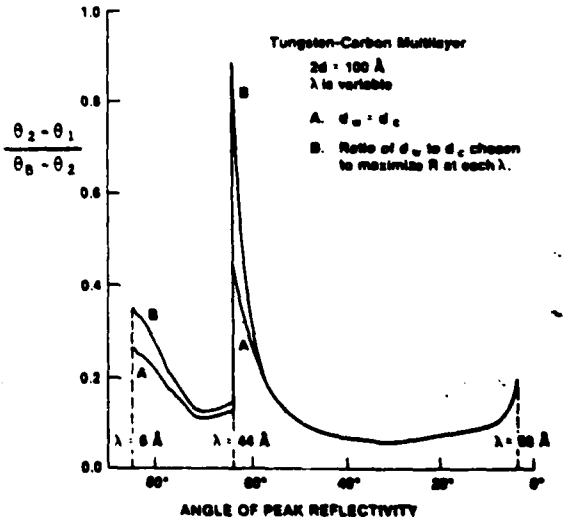

Fig. 5. Comparison of absorption correction to dispersion correction.

V. The Effect of Random Thickness Errors On Multilayer Reflectivity

Random thickness errors in an x-ray multilayer can cause a severe degredation in reflectivity. Even when the errors are small compared to the multilayer's 2d-spacing, they can cause a significant cumulative dephasing if not compensated for during the fabrication.

Previous theoretical analysis of the effect of random thickness errors is largely limited to the work of Shellan on optical Bragg reflectors.[7] Shellan treats thickness errors as a small perturbation in the structure of dielectric reflectors having a small coupling constant per cell. X-ray reflectors have a small coupling constant, but it may not be adequate to consider the errors in x-ray reflectors to be small perturbations that cause only a small degredation in reflectivity. In the soft x-ray regime it is also important to include absorption, which can be the major factor determining the reflectivity.

We have met these requirements using an analysis based on the amplitude recursion equation introduced above (eq. (5)). This equation is:

$$\rho_{K+1} = e^{-2i(\phi_K - \mu)}\,\frac{\rho_K - (i\gamma - p) - (i\gamma + p)\,\rho_K^2}{} \qquad (20)$$

We treat ϕ_K as a random variable with mean

$$\langle \phi_K \rangle = \pi - (2\pi \langle d_K \rangle / \lambda)\cos\theta \qquad (21)$$

and known variance $\langle \Delta\phi^2 \rangle$. In a bilayer reflector,

$$\langle \Delta\phi^2 \rangle = \frac{4\pi^2}{\lambda^2}\cos^2\theta\,(\langle \Delta L^2 \rangle + \langle \Delta H^2 \rangle) \qquad (22)$$

if the errors in the L and H layers are independent.

We make the problem analytically tractable by first dividing ρ_K into a deterministic and a non-deterministic part, $\rho_K = \langle \rho_K \rangle + \tilde{\rho}_K$, and then making use of the inequality:

$$\langle |\tilde{\rho}_K|^2 \rangle \;<\; \leq |\rho_K|^2 \rangle \;<\; 1 \qquad (23)$$

The right inequality is fairly strong in the soft x-ray regime, where absorption is fairly large. The right inequality is also particularly strong when $\langle \Delta\phi^2 \rangle \gg |\mu|$, since the reflectivity is then severely degraded by the thickness errors.

On the other hand, the left hand inequality becomes very strong when $\langle \Delta\phi^2 \rangle \ll |\mu|$, since $\langle \rho_K \rangle \cong \rho_K$ when the errors are small.

For these reasons $|\tilde{\rho}_K|$ is generally $\ll 1$; in our analysis we therefore neglect terms that are cubic or higher in $\tilde{\rho}_K$. Our approximation is accurate in the limits $\langle \Delta\phi^2 \rangle \gg |\mu|$ and $\langle \Delta\phi^2 \rangle \ll |\mu|$, but is also fairly accurate in the intermediate region.

In a similar way we treat the K-dependence of ρ_K and $\tilde{\rho}_K$ in an approximate way that is correct in the limits $\langle \Delta\phi^2 \rangle \ll |\mu|$, $\langle \Delta\phi^2 \rangle \gg |\mu|$, $K \ll |\mu|^{-1}$, or when the absorption is sufficiently large that $|\rho| \ll 1$.

The final result for a reflector with J-1 cells is:

$$\langle R_J \rangle = |\langle \rho_J \rangle|^2 \left\{ 1 + \frac{2\langle \Delta\phi^2 \rangle}{|1 - E_1|^2}\left[\frac{1 - e_J}{2\,\mathrm{Im}(\delta_1)}\right.\right. \qquad (24)$$

$$\left.\left. - \mathrm{Re}\left(\frac{E_1 - e_J}{\mathrm{Im}(\delta_1) + (u/2)}\right) + \frac{e^{4(J-1)\mathrm{Re}(u)} - e_J}{2\,\mathrm{Im}(\delta_1) + \mathrm{Re}(u)}\right]\right\}$$

where:

$$e_J \equiv e^{-4(J-1)\,\mathrm{Im}(\delta_1)} \qquad \gamma \equiv -i - (i\gamma - p)\langle \rho_1 \rangle$$

$$f \equiv 1 + \langle \Delta\phi^2 \rangle$$

$$\langle R_J \rangle = \frac{1}{2v}\left(2u\,\frac{1 + wE_J}{1 - wE_J} - 2f\right) \qquad (25)$$

$$w \equiv \frac{1 - (u/f)}{1 + (u/f)} \qquad E_J \equiv e^{-2(J-1)u} \qquad u \equiv \sqrt{f^2 - (i\gamma - p)v}$$

The accompanying figure shows $\langle R_J \rangle$ plotted as a function of RMS thickness error in a particular example.

We have tested the accuracy of the analysis by making a Monte Carlo simulation. A computer program is used to generate a large number of randomly perturbed multilayer stacks, and to compute their mean reflectivity. Sample results are shown in the plot. The plot also shows a computation of $\Delta\lambda/\lambda$ as a function of RMS thickness error.

There are no free parameters in the fit of the analytic expression to the Monte Carlo results.

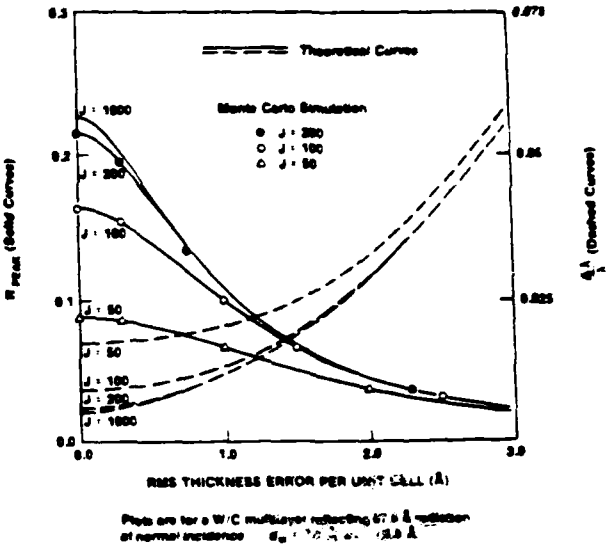

Fig. 6. Effect of random thickness errors on multilayer reflectivity.

VI. The Effect of Interfacial Roughness On Multilayer Reflectivity

Eastman has developed numerical methods to treat the effect of layer roughness in optical multilayers.[8] We have used similar physical assumptions to treat certain kinds of roughness in x-ray multilayers analytically. Our model assumes, in effect, that the near-field reflected beam above any point on the multilayer's surface can in principle be calculated by inserting local values for the layer properties into an algorithm that computes the reflectivity of multilayers with planar interfaces. Such a scalar model of the roughness requires that the transverse autocorrelation length of the roughness be large compared to the layer thicknesses. A more detailed discussion of the physical assumptions of the scalar model is given in ref. 8.

Ref. 9 discusses the limitations of scalar scattering theory in comparison with more rigorous theories. In general the scalar theory is best at predicting total specular and diffuse reflectivities

and at predicting the angular distribution of the diffusely reflected beam at angles close to the specular beam; it cannot predict polarization effects.

One kind of multilayer roughness that has been treated with the scalar theory is that which Eastman calls "identical films", in which all layers are considered to reproduce a common roughness profile (generally that of the substrate). The autocorrelation length of the roughness in the longitudinal direction is therefore very large. Spiller et al. and Haelbich et al. have discussed the effect of roughness on x-ray multilayer reflection in terms of the same expression as results from the identical film model.[10,11]

We have modeled two kinds of non-identical roughness in which the longitudinal autocorrelation length is very small, so that the roughness profiles of the different layers are uncorrelated. We refer to the two as "roughening films" and "smoothening films".

In the case of roughening films, we assume that the errors in the local layer thicknesses above each point on the surface cause a cumulative dephasing, so that the absolute roughness of the top layer increases in a random walk fashion as more layers are added. One may consider the formation of these films to be such that the granularity in each layer is independently added to a baseline of roughness established by preceeding layers.

Under the assumptions of the scalar model, the near-field amplitude is given by the equation for one-dimensional thickness errors discussed above. The far field coherent reflectance is obtained by evaluating:

$$R_{coh} = |\langle \rho_{far\ field} \rangle|^2$$

$$= |\ \text{Fourier transform}\{\langle \rho_{1D}(x) e^{2i \sum_{K=1}^{J-1} \Delta\phi(x)_K} \rangle\}|^2 \qquad (26)$$

Here x is a coordinate along the surface, and $\rho_{1D}(x)$ is the near-field amplitude as measured at the upper surface of the multilayer. This upper surface is rough, so the factor $\exp(2i\Sigma\Delta\phi_K)$ must be used to propagate $\rho_{1D}(x)$ to a mean plane, where the far-field amplitude can properly be evaluated via the Fourier transform.

The argument of the transform is independent of x, so R_{coh} will be a delta-function of the angle of reflection. R_{coh} can therefore be identified as the specular beam. Our expression for R_{coh} in the soft x-ray regime is given below (eq.(27)).

A diffuse beam is also present. The total intensity of the diffuse and specular beams is determined by the total absorption, which is the same as in the case of 1D thickness errors discussed above.

We have also developed an analytic model for the kind of roughness we call "smoothening films". Such films may be considered to have a leveling nature during some stage of formation, but to nonetheless possess an intrinsic roughness after formation is complete. We therefore assume that an error in the local thickness that a layer has at some position on the reflector will be compensated for in the thickness of the next layer deposited. The roughness height necessary to cause a given drop in reflectivity is therefore much larger than in the case of roughening films, because the thickness errors do not accumulate (see plot).

It turns out that the smoothening property of this type of roughness causes the intensities of the diffuse and specular beams to become equal only at a level of roughness where the total reflectivity has been decreased quite substantially (via an increase in absorption). In contrast, with roughening films, the two become equal at a roughness level where the total reflectivity is only slightly decreased. With identical films, the total reflectivity is unaffected by the magnitude of the roughness.

With films of both the roughening and smoothening types, the total absorption reaches a steady-state level as more and more layers are added. However in the case of roughening films the proportion of the reflected light in the specular beam steadily decreases, since the upper surfaces get steadily rougher.

The acceptance angle of multilayers with smoothening films is not greatly influenced by the RMS magnitude of the roughness. In the case of roughening films, the acceptance angle is increased in somewhat the same way as would be caused by an increase in the layer bulk absorption constants.

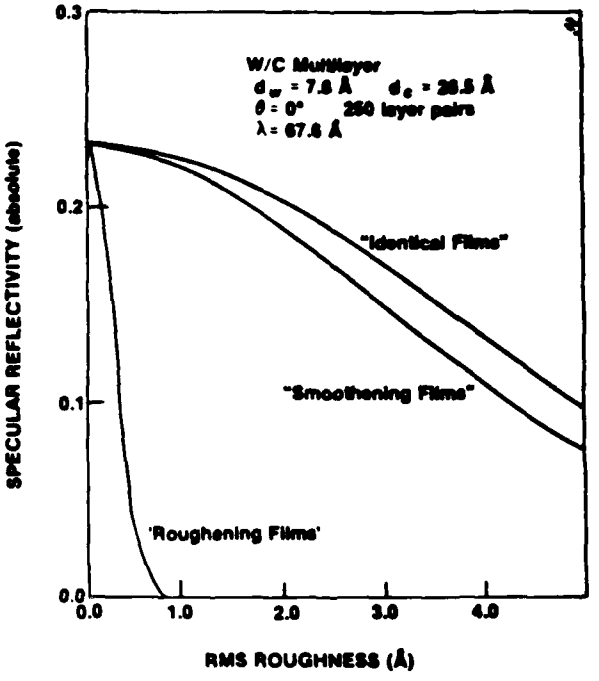

Fig. 7. Effect of roughness - reflection into specular beam.

Our expressions for specular reflection in the presence of roughness assume that the absorption has reached its steady-state value. Our expression for the case of smoothening films assumes a bilayer structure and Gaussian statistics for the roughness.

Our expression for roughening films is:

$$R_{coh} = |\langle \rho_{1D} \rangle F_1 \cdot \frac{2\langle \Delta\phi^2 \rangle \langle \rho_{1D} \rangle}{i\tilde{\delta} + \langle \Delta\phi^2 \rangle} (F_J - G_{J-1})$$

$$+ 2\langle \rho_{1D} \rangle G_J H_J (F^J - 1)|^2 \qquad (27)$$

where:

$$F_J \equiv e^{-2(J-1)\langle \Delta\phi^2 \rangle} \quad . \quad G_J \equiv e^{2i\tilde{\delta}(J-1)}$$

$$H_J \equiv e^{\frac{i\gamma + p}{i\,t + \langle \Delta\phi^2 \rangle}} \langle \rho_{1D} \rangle \qquad (28)$$

$\langle \rho_{1D} \rangle$ is given by eq. (25),
and the remaining symbols are as defined above.

For smoothening films, our result is

$$R_{coh} = \left| \frac{\gamma e^{-2\langle \xi^2 \rangle}}{\sqrt{t^2 - \gamma^2 e^{-4\langle \xi^2 \rangle}} - t} \right|^2 \qquad (29)$$

where $\langle \xi^2 \rangle = \frac{\pi^2 \sigma^2}{d^2}$ with σ the RMS roughness height in each interface, and where γ and t are as previously defined.

We note that the effect of smoothening films is very similar to that of interlayer diffusion. This is particularly true if the RMS roughness height is at least moderately small, so that $e^{-2\langle \xi^2 \rangle} \gg q|\mu|$, where q is the number of layers within one longitudinal autocorrelation length of the roughness. (The analysis assumes that $q|\mu| \ll 1$).

In this case the intensity of the diffuse beam will be small compared to that of the specular beam, even though the specular reflectivity may be considerably less than it would be in the absence of roughness. The main effect of the roughness in this case is to decrease the reflectivity of the multilayer, rather than to scatter radiation diffusely. This is because radiation that is diffusely scattered from different layers adds only incoherently under the assumptions of the smoothening film model.

For comparison, suppose one models the diffusion process by considering it to cause the ideal multilayer profile $\Delta(z)$ to be convolved with some diffusion profile $g(z)$.

This causes the parameter γ to be multiplied by the Fourier transform of $g(z)$. If g is taken to be a Gaussian, $g(z) = \exp(-.5(z/\sigma)^2)$, the reflected intensity is given by an expression identical to eq.(29) above for R_{coh} in the presence of smoothening films.

Ref. 8 gives an expression for specular reflectivity in the presence of identical films that applies under the assumptions of the scalar model. The same expression is used in ref. 11.

We also note that for all three types of roughness, walkoff considerations can be shown to imply that the scalar model is applicable only when the separation between the specular and diffuse beams is within the acceptance angle of the multilayer. Since the acceptance angle is likely to be of the order of the field of view in imaging applications, the scalar model can be applied to many imaging problems of interest.

Acknowledgements

This research was partially supported by the Air Force Office of Scientific Research, grant AFOSR-81-0059.

This research was also partially supported by the following sponsors: Exxon Research and Engineering Company, General Electric Company, Northeast Utilities, New York State Energy Research and Developement Authority, The Standard Oil Company of Ohio, The University of Rochester, and Empire State Electric Energy Research Corporation. Such support does not imply endorsement of the content by any of the above parties.

A.R. gratefully acknowledges the support of a Fannie and John Hertz Foundation Fellowship.

References

1) M.Born, E.Wolf, Principles of Optics, Pergamon, 1975.

2) Z.Knittl, Optics of Thin Films, Wiley, N.Y.&London, 1976.

3) A.V.Vinogradov and B.Ya.Zeldovich, Appl.Opt.16,89 (1977).

4) B.Henke, to be published.

5) F.Miller, Phys.Rev.47,209 (1935).

6) R.W.James, The Optical Principles of the Diffraction of X-Rays, G.Bell and Sons, London 1950.

7) J.B.Shellan et al., J.Opt.Soc.Am.68,18(1978).

8) J.Eastman, Physics of Thin Films, v.10, 1978, p. 167.

9) J.M.Elson et al., in Applied Optics and Optical Engineering, edited by R.R.Shannon and J.C.Wyant (Acad. Press, N.Y., 1979), Vol. VII, pp. 198,199.

10) E.Spiller, A.Segmüller, J.Rife, R.-P. Haelbich, Appl.Phys.Lett 37(11),1 Dec. 1980, p.1048.

11) R.-P. Haelbich, A.Segmuller, E.Spiller, Appl.Phys.Lett.34(3),1 Feb. 1979, p.184.

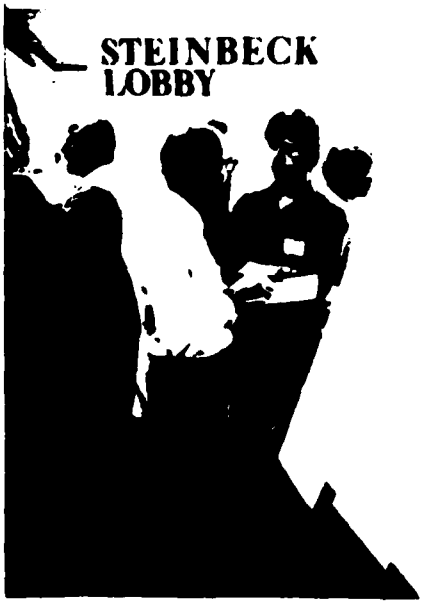

University of Rochester graduate student Alan Rosenbluth discussing his results with Dr. Eberhard Spiller of IBM.

Bragg condition in absorbing x-ray multilayers

Alan E. Rosenbluth
Laboratory for Laser Energetics, University of Rochester, 250 East River Road, Rochester, New York 14623
Ping Lee
University of California, Los Alamos National Laboratory, Los Alamos, New Mexico 87545

(Received 26 October 1981; accepted for publication 21 December 1981)

The angle of maximum reflectivity from a multilayer x-ray reflector is influenced by absorption in the medium. Using multilayer theory we show how the full refractive correction compares to the usual correction that includes only the effect of dispersion. The physical significance of the two corrections is discussed. The absorption correction is computed for some multilayer systems of current interest.

PACS numbers: 78.70.Ck, 78.70.Dm

Much progress has been reported recently in the fabrication of artificial Bragg reflectors for the soft x-ray regime.[1-5] Applications for these multilayer systems include monochromators for synchrotron radiation,[3] normal incidence mirrors for subkilovolt x-ray imaging systems,[6] grazing incidence mirrors for the reflection of higher energy x rays than is otherwise practical,[4] and cavity mirrors for future x-ray lasers.[7] In multilayers used with such devices, the wavelength (λ), glancing angle of incidence (θ), and period spacing (d) must be carefully matched.

It is well know that the simple Bragg relation

$$2d \sin\theta_B = m\lambda \tag{1}$$

must be corrected for refractive effects. The crystal plane spacing d and wavelength in vacuum λ are both measured in angstroms. θ_B is the grazing angle of incidence and the integer m is the order of diffraction. The standard treatment of the refraction correction in a perfect crystal ignores the effect of absorption.[8,9] Expressed in angular units, this standard correction for a crystal having a spatially averaged index of refraction $n = 1 - \bar{\delta} - i\bar{\beta}$ is

$$\theta - \theta_B = \bar{\delta}/\sin\theta_B \cos\theta_B, \tag{2}$$

where it is assumed that $\delta \ll 1$ and $\beta = 0$.

Equation (2) does not correctly give the position of maximum reflectivity in a system when n is complex. Shacklett and DuMond have suggested that the absorption correction be made graphically.[10] Miller has derived an analytic expression for the full refractive correction using the Darwin–Prins dynamical theory of crystal diffraction.[11] In this letter, the angular position of diffraction maxima have been obtained by simpler means, using a formalism developed to treat multilayer reflection.

We note that in many applications such as those cited above, the incident beam can be treated as linearly polarized. In a previous report,[12] it has been shown that in this case the intensity reflectance R of a multilayer containing a large number of layers is

$$R = |\rho|^2 = \left| \frac{-(D + iB)}{\xi - [\sqrt{\xi^2 - (D + iB)^2}]} \right|^2. \tag{3}$$

Here ρ is the amplitude reflectivity of the multilayer and $-(D + iB)$ is the amplitude reflectivity of a single priod. ξ is a detuning parameter defined in terms of the optical phase thickness Ψ of the multilayer's basic period through the relation

$$\xi = \Psi - m\pi \cong \frac{m\pi}{\sin\theta_B}\left((\sin\theta - \sin\theta_B) - \frac{\bar{\delta} + i\bar{\beta}}{\sin\theta} \right), \tag{4}$$

where we have defined

$$\Psi \equiv \frac{2\pi}{\lambda}\int_{\text{period}} dz\, n(z)[\sqrt{1 - \cos^2\theta/n^2(z)}]$$
$$\cong \frac{2\pi d \sin\theta}{\lambda}\left(1 - \frac{\bar{\delta} + i\bar{\beta}}{\sin^2\theta}\right), \tag{5}$$

with z the coordinate perpendicular to the layer interfaces. The second part of Eq. (5) follows because $|n(z) - 1| \ll 1$ in the x-ray regime.

In Ref. 12, the parameters $D + iB$ and $\bar{\delta} + i\bar{\beta}$ are derived for multilayers consisting of alternating layers of two materials having indicies of refraction n_1 and n_2. $\bar{\delta}$ and $\bar{\beta}$ are the averaged unit decrements given by $\bar{\delta} = \gamma\delta_1 + (1 - \gamma)\delta_2$ with similar expression for $\bar{\beta}$, where γ is the division parameter defined by $\gamma \equiv d_1/(d_1 + d_2)$. $D + iB$ equals $-(-1)^m 2r \sin(m\pi\gamma)$, where r is the Fresnel reflection coefficient. To first order in the unit decrement differences, r is given by

$$r = [(\Delta\delta + i\Delta\beta)/2\sin^2\theta]P(\theta), \tag{6}$$

where $P(\theta) = 1$ or $\cos(2\theta)$ depending on whether the incident beam is S polarized or P polarized, respectively, and $\Delta\delta + i\Delta\beta \equiv (\delta_1 + i\beta_1) - (\delta_2 + i\beta_2)$.

We now calculate the positions of maximum reflectivity. D and B are virtually independent of ξ, since $\theta \cong \theta_B$, so that using Eq. (3),

$$\frac{1}{2R}\frac{dR}{d\theta} = \mathrm{Re}\left(\frac{1}{\rho}\frac{d\rho}{d\xi}\frac{d\xi}{d\theta}\right) \cong f\,\mathrm{Re}\left(\frac{1}{\rho}\frac{d\rho}{d\xi}\right) = f\,\mathrm{Re}(Y^{-1}), \tag{7}$$

where

$$Y \equiv [\sqrt{\xi^2 - [2r\sin(m\pi\gamma)]^2}]$$

and

$$f \equiv \frac{m\pi\cos\theta}{\sin\theta_B} \cong \frac{d\xi}{d\theta}. \tag{8}$$

In Eqs. (8) and (3) the root with the positive imaginary part must be chosen.

 0003-6951/82/060466-03$01.00

At $dR/d\theta = 0$, the reflectivity is maximized. Therefore, the positions of the diffraction maxima can be obtained from the condition

$$\mathrm{Re}\, Y = 0, \tag{9}$$

where we have used the identity $\mathrm{Re}(Y^{-1}) = |Y|^{-2}\,\mathrm{Re}\,(Y)$.

It is shown in Ref. 13 that the variable

$$\Phi_e = m\pi - Y \tag{10}$$

is the quantity known as the equivalent phase thickness, that has been introduced into multilayer analysis by Herpin.[14]

Equation (9) is, therefore, a requirement that the real part of the multilayer's equivalent phase thickness equal $m\pi$ at the position of maximum reflectivity. This is not the same as the conventional requirement that the real part of the optical phase thickness Ψ equal $m\pi$.

We may explain the difference as follows. The oscillation of the forward traveling wave across each period of the multilayer is given by $e^{-i\Phi_e}$, since Φ_e is the equivalent phase thickness. This oscillation is determined not only by the optical phase thickness of the period being traversed, but also by multiple reflections involving the other periods of the multilayer.

This may be seen by eliminating the radical in the denominator of Eq. (3) to obtain

$$\rho = -(\xi + Y)/(D + iB), \tag{11}$$

so that $Y = -\xi - \rho\,(D + iB)$ and

$$\Phi_e = \psi + \rho\,(D + iB), \tag{12}$$

and therefore

$$e^{-i\Phi_e} = e^{-i\psi}\,[1 - i\rho\,(D + iB)] + 0(r^2). \tag{13}$$

Here the term $e^{-i\psi}$ represents the effect of transmission through the period. The term $-e^{-i\psi}\rho i(D + iB)$ represents a multiple reflection process consisting of transmission through the period, reflection from all succeeding periods, and reflection back into the initial direction by the period initially traversed. (Higher-order multiple reflections are of order r^2 and are small.) A phase change occurs during the multiple reflection, and if n is complex, the overall oscillation of the field across the period is shifted. For brevity's sake, we have described the calculation of this effect as a correction for absorption.

We can convert the resonance condition of Eq. (9) to a computationally more useful form as follows: The condition $\mathrm{Re}\, Y = 0$ implies that Y^2 must be a negative real number. It is readily shown that the condition $\mathrm{Im}(Y^2) = 0$ is sufficient to ensure $\mathrm{Re}(Y^2) < 0$. From Eqs. (8) and (6), the requirement that $\mathrm{Im}(Y^2) = 0$ yields

$$(\sin\theta - \sin\theta_B)\sin\theta = \bar{\delta} - \frac{\Delta\delta\Delta\beta\,\sin^2(m\pi\gamma)P^2(\theta_B)}{m^2\pi^2\bar{\beta}}, \tag{14}$$

where we have set $P(\theta) \cong P(\theta_B)$. Introducing $\Delta\theta \equiv \theta - \theta_B$ and using

$$(\sin\theta - \sin\theta_B)\sin\theta = \Delta\theta\,(\cos\theta_B - \tfrac{1}{2}\Delta\theta\sin\theta_B)\sin\theta_B + 0(\Delta\theta^2\cos^2\theta_B) \tag{15}$$

(which is accurate even near normal incidence where the two terms in the first parentheses on the right may be comparable), we find that $\Delta\theta$ is given by

$$\Delta\theta = \{1 - [\sqrt{1 - 2\eta\sec^2\theta_B}\,]\}/\tan\theta_B, \tag{16}$$

where η is defined to be the right-hand side of Eq. (14).

Equation (16) is valid for all angles outside the grazing incidence regime, except that no physical solution exists if the radicand on the right side is negative, which, to a good approximation, can be assumed to occur if $\theta_B > \pi/2 - (\sqrt{2\eta})$.

Away from normal incidence [i.e., $\pi/2 - \theta_B \gg (\sqrt{2\eta})$], Eq. (16) can be written as

$$\Delta\theta = \frac{\bar{\delta}}{\sin\theta_B\cos\theta_B} - \frac{\Delta\delta\Delta\beta\,\sin^2(m\pi\gamma)P^2(\theta_B)}{m^2\pi^2\bar{\beta}\sin\theta_B\cos\theta_B}. \tag{17}$$

The first term is the usual dispersion correction. The second term is due to absorption.

Equation (16) can be applied to a general noncentrosymmetric structure (such as a crystal) by letting $\eta = \bar{\delta} - (D\bar{B} + \bar{D}B)\sin^4\theta_B/(2m^2\pi^2\bar{\beta})$. D, B, $\bar{D}$, and $\bar{B}$ are standard parameters of crystal diffraction theory, whose use in multilayer analysis is discussed in Ref. 12.

In the common case of a crystal that is centrosymmetric, Eq. (17) may be applied in the form

$$\Delta\theta = \frac{\bar{\delta}}{\sin\theta_B\cos\theta_B} - \frac{[r_0\mathcal{N}\lambda/2\pi]^2F_1F_2P^2(\theta_B)}{\bar{\beta}\sin\theta_B\cos\theta_B}. \tag{18}$$

Here F_1 and F_2 are the real and imaginary parts, respectively, of the crystal structure factor. r_0 is the classical electron radius and $\mathcal{N}$ is the reciprocal of the unit cell volume.

The relative magnitude of the two corrections are compared in Fig. 1 for the case of a particular reflecting structure. The ratio plotted is

$$\mathrm{RATIO} = (\theta_1 - \theta_2)/(\theta_2 - \theta_B), \tag{19}$$

where θ_2 is the true Bragg angle as corrected for absorption and dispersion and θ_1 is the Bragg angle as corrected for

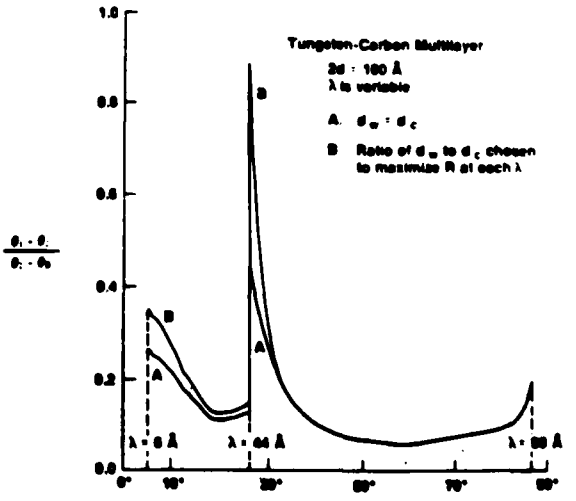

FIG. 1. Comparison of absorption correction to dispersion correction versus angle of peak reflectivity.

TABLE I. Calculated diffraction peak positions in degrees for oxygen-$K\alpha$ line, $\lambda = 23.6$ Å.

	θ_2	θ_B	Refraction correction	Absorption correction	Ratio (%)
Vanadium/carbon (multilayer*)	13.910 3	13.621 1	0.263 8	0.031 3	− 10.61
Tungsten/carbon (multilayer*)	14.317 4	13.621 1	0.869 1	− 0.139 0	19.04
TlAP (crystal)	65.826 37	65.671 29	0.164 28	− 0.009 57	6.19
RAP (crystal)	65.444 46	65.283 96	0.164 02	− 0.003 80	2.37
KAP (crystal)	63.000 39	62.859 98	0.140 98	− 0.000 74	5.28
NAAP (crystal)	63.421 85	63.286 17	0.135 73	− 0.000 19	0.14
NHAP (crystal)	64.433 82	64.304 00	0.130 36	− 0.000 71	0.55

*$2d = 100$ Å and $\gamma = 0.5$.

dispersion only. Equation (19) is the ratio of the absorption correction to the net correction.

To obtain Fig. 1, we have used preliminary values of atomic scattering factors from a forthcoming compilation.[15]

One can show that the absorption correction must always be smaller than the dispersion correction, but the plot shows that there are regimes in which the two effects are comparable to order of magnitude.

First, the absorption has an increased effect on the resonance angle near normal incidence, where the correspondence between angular shifts and shifts in phase thickness is nonlinear.

Also, the absorption correction is comparatively large at wavelengths just above the carbon K edge, and a short wavelengths; in these regions the effect of multiple reflections is comparatively strong.

Table I shows the refraction and absorption corrections associated with reflection from other periodic structures. In all cases $m = 1$ and $\lambda = 23.6$ Å (oxygen $K\alpha$ line). θ_2 is the predicted diffraction peak position, valid to all orders of $\Delta\theta$, computed using Eq. (14). The refraction and absorption corrections are the first and second terms of the right-hand side of Eq. (17), respectively. The difference between the θ_2 column and the sum of the next three columns reflects the contribution of higher order $\Delta\theta$ terms which have been ignored in Eq. (17).

Finally, the last column is the ratio, Eq. (19), in percent of absorption correction to the net correction. As long as the refractive indices have real parts less than 1, the refraction correction always adds to the Bragg angle θ_B. The absorption correction generally subtracts from θ_B; however, there are cases where absorption adds to θ_B as is evident in the case of the vanadium/carbon multilayer.

The authors wish to thank B. L. Henke and J. M. Forsyth for many useful conversations. A. R.'s research was partially supported by the Air Force Office of Scientific Research, Grant AFOSR-81-0059. A. R.'s research was also partially supported by the following sponsors: Exxon Research and Engineering Company, General Electric Company, Northeast Utilities, New York State Energy Research and Development Authority, The Standard Oil Company of Ohio, and Empire State Electric Energy Research Corporation. Such support does not imply endorsement of the content by any of the above parties. Finally, A. R. gratefully acknowledges the support of a Fannie and John Hertz Foundation Fellowship.

[1]T. W. Barbee, Jr. and D. C. Keith, Stanford Synchrotron Radiation Laboratory Report No. 78104, 1978, pp. III-26.
[2]R. P. Haelbich, A. Segmuller, and E. Spiller, Appl. Phys. Lett. 34, 184 (1979).
[3]B. L. Henke, Nucl. Instrum. Meth. 177, 187 (1980).
[4]L. N. Koppel and T. W. Barbee, Jr., Lawrence Livermore National Laboratory Report No. UCRL-85817, 1981.
[5]E. Spiller, A. Segmuller, J. Rife, and R. P. Haelbich, Appl. Phys. Lett. 37, 1048 (1980).
[6]E. Spiller, Nuc. Instrum. Meth. 177, 187 (1980).
[7]R. C. Elton, in *Advances in X-Ray Analysis*, edited by Barrett *et al.* (Plenum, New York, 1978), Vol. 21.
[8]A. H. Compton and S. K. Allison, *X-Rays in Theory and Experiment*, 2nd ed. (Van Nostrand, New York, 1935).
[9]R. W. James, *The Optical Principles of the Diffraction of X-Rays* (Cornell University, Ithaca, New York, 1965), p. 168.
[10]R. L. Shacklett and J. W. M. DuMond, Phys. Rev. 106, 501 (1957).
[11]F. Miller, Jr., Phys. Rev. 47, 209 (1935).
[12]P. Lee, Opt. Commun. 37, 159 (1981).
[13]A. E. Rosenbluth and J. M. Forsyth, in *Proceedings of the Topical Conference on Low Energy X-ray Diagnostics*, (AIP, New York, to be published).
[14]A. Herpin, Compt. Rendu. 225, 182 (1947) (French); see also Z. Knittl, *Optics of Thin Films* (Wiley, New York, London, 1976).
[15]B. L. Henke, P. Lee, T. J. Tanaka, R. L. Shimabukuru, and B. K. Fujikawa, Atomic and Nuclear Data Table 27 (1982).

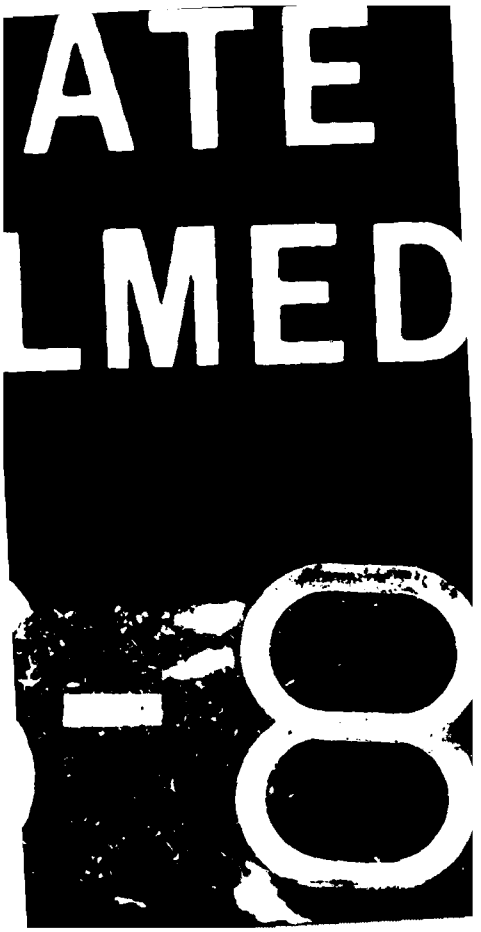
ATE
LMED
8